Check for updates

RESEARCH ARTICLE

ADVANCED ENERGY MATERIALS
www.advenergymat.de

Pizza Oven Processing of Organohalide Perovskites (POPOP): A Simple, Versatile and Efficient Vapor Deposition Method

Quentin Guesnay, Florent Sahli, Kerem Artuk, Deniz Turkay, Austin G. Kuba, Nada Mrkyvkova, Karol Vegso, Peter Siffalovic, Frank Schreiber, Huagui Lai, Fan Fu, Martin Ledinský, Nicolas Fürst, Aymeric Schafflützel, Cédric Bucher, Quentin Jeangros, Christophe Ballif, and Christian M. Wolff**

Hybrid vapor deposition is one of the most appealing processes for perovskite photovoltaics fabrication, thanks to its versatile nature. By using sequentially different vapor deposition processes tailored to the inorganic and organic perovskite precursors' peculiarities, this type of process gives access to the full potential of vapor deposition. While vapor deposition of metal halides is well understood and mastered, vapor deposition of organohalide species is much more delicate (degradation of vapors, high vapor pressure, setup-specific constraints). Here, a novel close space sublimation system is reported and in-depth insights on the conversion into perovskite of a metal halide template are provided. In this evolution of the process, the substrate coated with metal halide template and the organohalide source are loaded together in a dedicated holder, then transferred into a vacuum chamber on a heating element already at temperature setpoint. The system enables a simple, fast, low-cost, and easy-to-reproduce organohalide vapor deposition process. The formation of the perovskite in situ and identification different conversion regimes are studied. Furthermore, the influence of the chemical environment and chamber design on the process are discussed. Compositional tuning and additive engineering in the process are processed and fabricate proof of concept photovoltaic devices reaching high fill factors of 80% and 17% power conversion efficiency for a bandgap of 1.63 eV.

1. Introduction

Within about a decade after their first demonstration, perovskite photovoltaics has emerged as a critical research field for renewable energy. Thanks to their potential to be processed at low costs,[1,2] a large bandgap tunability[3,4] and recent demonstration of lab-scale photovoltaic devices reaching 26% power conversion efficiency in single junction and 33.7% in tandem devices with crystalline silicon (c-Si) bottom solar cells,[5] perovskite thin films turn out to be one of the most promising ways toward the next generation of commercial solar cells. By taking advantage of the already existing c-Si solar cells production lines (with c-Si cells representing more than 95% of the market[6]), a perovskite deposition add-on would offer the easiest way to 30% efficient commercial solar modules.

Most vapor phase processes allow the deposition of conformal coatings, covering, e.g., the micrometer-sized pyramids

---

Q. Guesnay, K. Artuk, D. Turkay, A. G. Kuba, N. Fürst, C. Bucher, C. Ballif, C. M. Wolff
Ecole Polytechnique Fédérale de Lausanne (EPFL)
Institute of Electrical and Microengineering (IEM)
Photovoltaics and Thin-Film Electronics Laboratory
Neuchâtel 2002, Switzerland
E-mail: quentin.guesnay@epfl.ch; christian.wolff@epfl.ch

F. Sahli, A. Schafflützel, Q. Jeangros, C. Ballif
CSEM
Sustainable Energy Center
Neuchâtel 2002, Switzerland

N. Mrkyvkova, K. Vegso, P. Siffalovic
Institute of Physics
Slovak Academy of Sciences
Dúbravská cesta 9, Bratislava 845 11, Slovakia

N. Mrkyvkova, K. Vegso, P. Siffalovic
Center for Advanced Materials Application
Slovak Academy of Sciences
Dúbravská cesta 9, Bratislava 845 11, Slovakia

F. Schreiber
Institute of Applied Physics
University of Tübingen
72076 Tübingen, Germany

The ORCID identification number(s) for the author(s) of this article can be found under https://doi.org/10.1002/aenm.202303423

DOI: 10.1002/aenm.202303423

© 2024 Wiley-VCH GmbH

of state-of-the-art silicon solar cells. They are also free from toxic solvents, so they are adapted to implementation in already existing large-scale production lines. However, hybrid organic–inorganic lead halide perovskites, demonstrating the highest performances, are delicate to evaporate. Complexity arises from the different behaviors of inorganic and organic precursors upon evaporation. While the vapor deposition of inorganic halide precursors is relatively straightforward, vapor deposition of organohalides is more challenging because of their high vapor pressure and inclination to degradation.[7–11]

Hybrid vapor deposition processes combine two different vapor techniques: one adapted to metal halide deposition and another designed to best cope with the peculiarities of organohalides. Whereas already existing vapor processes (such as thermal evaporation or magnetron sputtering) are well adapted to metal halides, there is a need for the development of a vapor deposition process of organohalides, capable of converting metal halide templates into large-scale, uniform, and high-quality perovskite thin films with process durations of industrial relevance.[12]

To tackle these challenges, Sahli et al. presented a vapor transport deposition system featuring a separated evaporator and deposition chamber.[13] Organohalide vapors, generated by heating under vacuum, are transported from the evaporator to the deposition chamber by a carrier gas through a network of pipes and dispensed on the samples via a showerhead. All process parameters (different temperatures, pressure, carrier gas flux etc.) are decorrelated and independently controlled. The setup's capabilities were demonstrated by homogeneously coating an industrially standard 6-inch (239 cm^2) textured silicon wafer with a methylammonium lead tri-iodide ($MAPbI_3$) perovskite layer. Still, the transition to depositing formamidinium (FA) as the organic cation for the high-performing perovskites is more complicated because of the degradation of the organohalide vapors both during evaporation[11] and transport.[10] Here, replacing the inert nitrogen carrier gas with ammonia to mitigate the degradation of FA vapors was proposed, enabling the formation of FA-based halide perovskites, albeit only after several hours of vapor exposure.[10]

Here, we present a fast, low-cost, simple, and easy-to-reproduce advancement over the previous processes (Pizza Oven Processing of Organohalide Perovskites, POPOP). We study the perovskite formation in this process from a structural (in situ Grazing Incidence Wide Angle X-ray Scattering, GIWAXS), an optoelectronic (in- situ PhotoLuminescence, PL; PhotoLuminescence Quantum Yield, PLQY) and a chemical (Nuclear Magnetic Resonance, NMR; Fourier-Transform InfraRed spectroscopy, FTIR) perspective. We elucidate the influence of deposition parameters, mechanical design and chemical environment within the reaction chamber on thin film growth. Bandgap tuning and growth modulation via additive addition are demonstrated before implementing the developed thin films into perovskite solar cells.

2. Presentation of the Process

The first iteration of the in-house developed vapor deposition chamber[13] was designed with the objective of decoupling the evaporation and the deposition of the organohalides as much as possible. This entails a physical separation of the two processes. Consequently, evaporation was performed outside the deposition chamber, and a nitrogen carrier gas guided the as-generated vapors through a pipe network to the chamber. This design choice is prevalent among industrially mature chemical vapor deposition processes,[14–16] as it offers a straightforward approach for upscaling. The overall process flow, including the previous deposition of the metal halide template via co-evaporation, is depicted in Figure S1 (Supporting Information).

In the case of perovskite vapor deposition, this approach is accompanied by limitations to the process development. While working reasonably well with methylammonium (MA) based perovskites, formamidinium (FA) based perovskite cannot be deposited with the original process. As demonstrated in Figure S2 (Supporting Information), the thermally evaporated metal halide template (200nm of PbI_2: CsBr co-evaporated at 1 and 0.1 Ås^{-1} , respectively) cannot be converted into FA perovskite, under a wide variety of process parameters. More details on the metallic template vapor deposition are available in the methods section, and extensive characterization of our co-evaporated template has been reported in another study.[17] The only change detected in the thin films after the process is a strong presence of NH_4I. Suspecting the transport pipes as the origin of the lack of conversion, we reduced the pipe path from the evaporator to the reaction chamber (Figure S3, Supporting Information). This approach enabled the formation of FA-perovskites, albeit still limited by a long process duration and residual presence of NH_4I. We also observed that a complete template conversion into perovskite could be achieved if the substrate is directly positioned in the evaporator.

We conclude that the formamidinium vapors degrade along the path through the pipe scaling with the path length. This could be provoked by the high temperatures of the pipes (heated at 200°C after process optimization to prevent direct condensation of organohalide salts in the pipes) or FA degrading into several byproducts upon heating.[10,11] We consequently designed a setup with minimal substrate to organohalide distance and designed a microreactor based on polytetrafluoroethylene (PTFE) for its chemical inertness after carrying out a detailed study (Section: *Influence of chemical environment* and Figures S4– S8, Supporting Information) showing the effect of different materials in the vicinity of the reaction volume (two grades of stainless steel, PTFE, polyimide, aluminum foil). Moreover, short distances and small reaction volumes promote faster reactions, a critical parameter to reduce takt time for perovskite vapor deposition processes in an envisaged production line.[12]

In a last design modification, we aimed to reduce the heat-up time to a minimum and start the reaction quasi-instantly by placing precursors and substrate in a reaction chamber maintained at a temperature setpoint. A constant temperature without

---

H. Lai, F. Fu
Laboratory for Thin Films and Photovoltaics
Empa – Swiss Federal Laboratories for Materials Science and Technology
Dübendorf 8600, Switzerland

M. Ledinský
Laboratory of Thin Films
Institute of Physics
ASCR, Cukrovarnická 10, Prague 162 00, Czech Republic

© 2024 Wiley-VCH GmbH

16146840, 2024, 10, Downloaded from https://onlinelibrary.wiley.com/doi/10.1002/aenm.202303423 by UniversitÃ¤tsbibliothek TÃ¼bingen, Wiley Online Library on [08/03/2024]. See the Terms and Conditions (https://onlinelibrary.wiley.com/terms-and-conditions) on Wiley Online Library for rules of use; OA articles are governed by the applicable Creative Commons License

16146840, 2024, 10, Downloaded from https://onlinelibrary.wiley.com/doi/10.1002/aenm.202303423 by Universitätsbibliothek Tübinge, Wiley Online Library on [08/03/2024]. See the Terms and Conditions (https://onlinelibrary.wiley.com/terms-and-conditions) on Wiley Online Library for rules of use; OA articles are governed by the applicable Creative Commons License

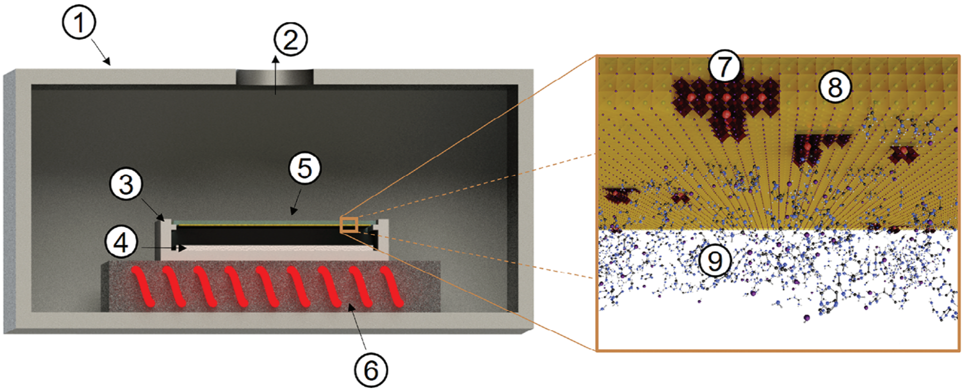

Figure 1. Schematic of the process. 1) Vacuum chamber 2) Opening leading to the pump 3) POPOP-Holder, comprising 4) Organohalide source (powder, pellet, dried solution, etc) 5) Substrate facing down and 6) Heating stage. Inset shows 7) Growing perovskite clusters emerging from the 8) Metal halide template exposure to the 9) Organohalide vapors.

complicated heating/cooling profiles simplifies the process, making it less error-prone and easier to reproduce. Lastly, loading the precursors at a given temperature setpoint, if high enough, allows the mixing of precursors with different boiling points and exposing the substrates almost simultaneously to all species. For example, a vapor additive could be provided to the growing thin film all along the process, whereas a heating profile starting from room temperature would unevenly disperse chemical species following their different phase transitions at a given temperature/pressure.

To combine all these advantages, i.e., initiating the reaction without delay due to transfer or pre-heating, reducing the vapor transport path length to a minimum, and ease of handling, we developed a method in which the reaction enclosure - constituting the lead halide template on a substrate, the holder made from PTFE and the organohalide powder delivery system - is premounted and subsequently transferred as one unit into a vacuum oven at a temperature setpoint that reaches its vacuum state ($p \approx 10^{-1}$ mbar) within seconds.

All these principles together lead to a concept reminiscent of the craftsmanship of a pizzaiolo, coining the name of the process: *Pizza Oven Processing of Organohalide Perovskites (POPOP)*. A mild vacuum environment is an attractive compromise between high vacuum and ambient. Unlike the latter, it provides control of the atmosphere and promotes the diffusion of the vapors, promising enhanced homogeneity. However, pumping time is only in the range of seconds, while reaching a high vacuum in a chamber large enough for vapor deposition takes dozens of minutes. A proof of concept prototype is developed and consists of a hollow PTFE cube, with formamidinium iodide (FAI) powder dispersed in it and holding a substrate covered with a metal halide template (PbI_2 alloyed with CsBr, details in Expeimental Section) facing downwards. A schematic of the process is shown in **Figure 1**. A drawing of the holder prototype is shown in Figure S9 (Supporting Information).

Several process conditions were varied and repeated (mass of loaded FAI, duration of the process and substrate to precursor distance) to assess the repeatability and controllability of the approach. The produced thin films were then analyzed by X-ray diffraction (XRD), Ultraviolet to Visible Absorption Spectroscopy (UV–vis) and PhotoLuminescence Quantum Yield measurements (PLQY), with the results presented in **Figure 2**. The simple prototype allows for the repeatable and controllable fabrication of perovskite films, albeit with low throughput (one 2.5 × 2.5 cm^2 sample for any given condition).

We showcase three different conditions representative of a larger set of conditions tested. In particular, from condition no. 1–3, we see a reduction in XRD signals assigned to the template (10° & 13°) coinciding with an increase in perovskite signal (14°). At the same time, we observe significant differences in the PLQY (ca. one order of magnitude higher PLQY for condition no. 3 vs. condition no. 2) of the films converted under these different conditions.

The absorptance, however, appears nearly identical for the different conditions. Scanning Electron Microscope (SEM) images and NMR spectra (Figure S9, Supporting Information), show no apparent differences in the film morphology, and the NMR spectra show no additional signal except FA signal without any other undesired species, irrespective of the process conditions.

3. In Situ Study of Thin Film Growth

The abovementioned ex situ measurements after the conversion process suggest different conversion stages depending on the process conditions (temperature, duration, mass of organohalides, etc.) are reflected in differences in the crystallographic and optoelectronic properties. We sought to follow the evolution from template to perovskite by making use of the in situ capabilities of GIWAXS,[18] and combining it with optoelectronic insights from photoluminescence monitoring, as proposed by Mrkyvkova and Held et al.[19–21]

The reaction chamber for the in situ setup is designed to mimic the reference chamber closely, yet one notable difference between the setups is the temperature profile. To exclude artefacts introduced hereby, we compared films reacted with different temperature profiles, either with a progressive heating profile or the reference flat temperature profile in Figure S11 (Supporting Information) after the same reaction times. From a structural (XRD), optoelectronic (PLQY), and chemical (NMR) point of view, the thin films produced with these two temperature profiles exhibit nearly identical results for all probed stages of conversion. Furthermore, intensity tests of the X-ray beam and laser

© 2024 Wiley-VCH GmbH

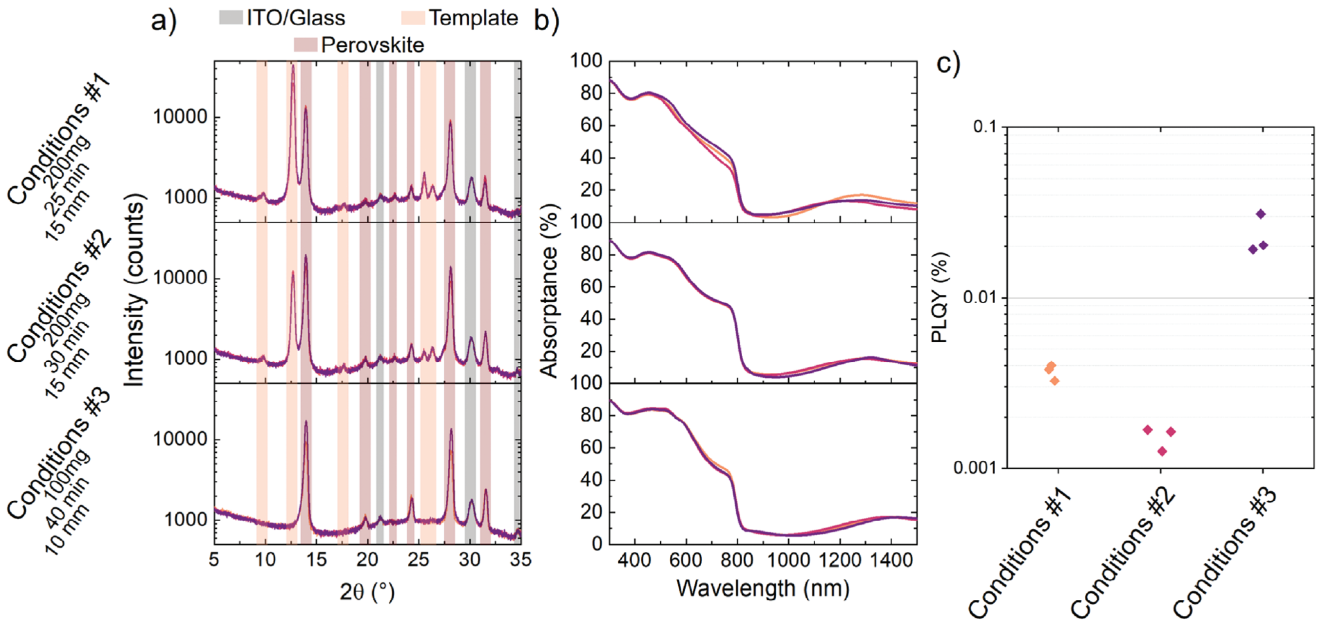

Figure 2. Investigation of the process repeatability. The process is run at the same conditions three times for three different sets of process parameters (200mg FAI/25min vapor exposure/15mm between substrate and salts, 200mg/30min/15mm and 100mg/40min/10mm) for a total of nine separate runs. a) XRD, b) Absorptance and c) PLQY are measured. The simple proof of concept prototype produces films with repeatable structural, optoelectronic and chemical properties.

excitation were made to exclude any detrimental influence (observer effect) on the in situ monitoring. The X-ray fluence was 10^8 photons/cm^2/s, two orders of magnitude below 10^{10} suggested by Held et al.[19] to prevent degradation and well below the 10^{16} decomposition threshold reported by Svanström et al.[22] We did not observe a degradation by illumination either, by comparing the evolution under continuous and discontinuous (30s off, 5s on) light illumination, Figure S12 (Supporting Information). Note, the in situ experiments were conducted with a temperature setpoint at 170°C, enabling a slightly decelerated reaction, allowing for more precise tracking and a faster heating to setpoint, despite the smaller heater.[23]

An exemplary in situ run is displayed in **Figure 3**. The reaction process can be divided into four stages. The first stage (0–10 min.) is the initialization stage: the temperature reaches ca. 75% of its target (125°C vs. 170°C). The GIWAXS signal stemming from the metal halide template does not show major changes and only a weak luminescent signal from the inorganic template[24] is detected. The thermal expansion of the system marks the second stage (10–30 min.), evident from the shift of all the reflected and diffracted X-rays to lower q. The expansion invokes a slight deviation from initial grazing conditions, affecting the signals, and limiting the information drawn from GIWAXS here. On the other hand, the photoluminescence signal displays a significant increase in intensity after ≈ 10 min with an emission peak emerging at a photon energy of ≈ 1.8 eV that then gradually shifts to lower energies. In other in situ monitoring of perovskite growth, this PL behavior marks the perovskite nucleation featuring highly emissive perovskite clusters, as confirmed by X-ray diffraction.[19,25–27]. In our case, identification of GIWAXS perovskite signal in stage two is made complicated by three factors: the much lower X-ray fluence (chosen to minimize observer effect), the departure from grazing incidence broadening the signal (due to thermal expansion of the holder) and intrinsic geometrical broadening due to measurement conditions.[28] Yet, the evolution of PL matches unambiguously the behavior reported in the previously cited studies, measuring X-ray diffraction in more favorable conditions.

In stage three, the clusters coalesce and the main perovskite formation occurs. The metal halide template signal gradually decreases, while the perovskite signal progressively increases (GIWAXS data, blends over after ≈ 35 min.). The PL peak energy drops to ≈ 1.6 eV and the signal drops by one order of magnitude. This can be explained by the fact that as the conversion progresses, the initially isolated perovskite crystallites spread and merge into a polycrystalline structure. The fading lead iodide passivates less and less as the perovskite is converted, and the as-formed domain boundaries embody non-radiative recombination centers,[29] hence decreasing the luminescence. Two factors influence the position of the photoluminescence emission: changes in perovskite cluster size (with an inversely proportional relationship, cf. quantum confinement)[19,26,27,30] and halide exchange (more iodine incorporation decreases the bandgap). Regarding the fading quantum confinement effect redshifting the bandgap in stage 2, an estimation of the perovskite cluster size using Brus' equation[31] gives a monotonic increase from 8 to 21 nanometers of the perovskite cluster diameter during this stage (cf. Figure S13). These values are coherent with the previously cited studies.[19,26,27,30] A mild blueshift is visible between 30 and 55 minutes. We attribute this phenomenon to the presence of bromine in the metal halide template (from CsBr alloying), probably diffusing from template to perovskite during growth and provoking a halide exchange.[32,33] Other in situ monitoring studies using a pure iodine metallic scaffold for their perovskite do

© 2024 Wiley-VCH GmbH

16146840, 2024, 10, Downloaded from https://onlinelibrary.wiley.com/doi/10.1002/aenm.202303423 by Universitätsbibliothek Tübinge, Wiley Online Library on [08/03/2024]. See the Terms and Conditions (https://onlinelibrary.wiley.com/terms-and-conditions) on Wiley Online Library for rules of use; OA articles are governed by the applicable Creative Commons License

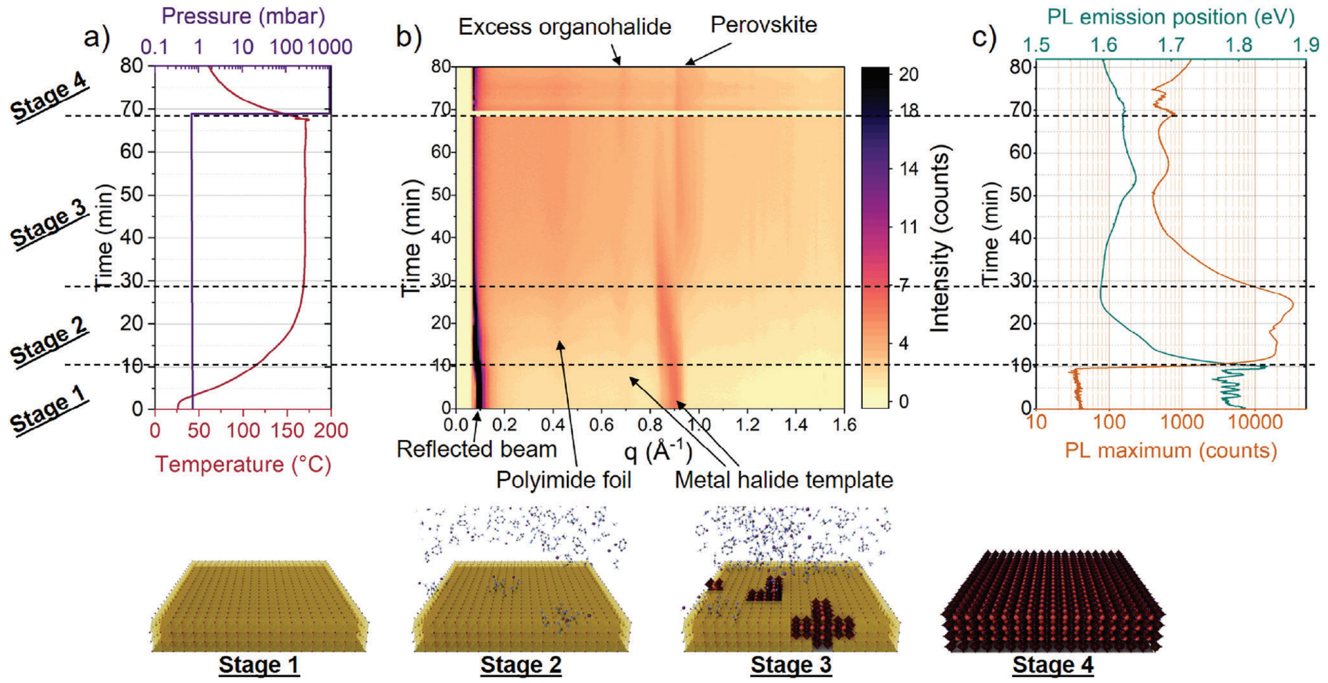

Figure 3. In situ GIWAXS & PL monitoring of the metal halide template converting into perovskite upon reacting with FAI. a) Pressure and temperature profiles, b) Azimuthally integrated GIWAXS profiles and c) Evolution of PL emission intensity and peak energy position. Four different stages are identified: 1) Heating up, template luminescence 2) Thermal expansion of the holder (cf. reflected beam shift) and formation of highly emissive perovskite clusters undetected via GIWAXS 3) Bulk formation of perovskite and consumption of metal halide template and 4) interruption of heating and exposure to ambient air.

not exhibit such 'late' blueshift during conversion.[19,25–27] Meanwhile, the continuous exposure to FAI vapors encourages a redshift via halide exchange, seemingly dominant from 55 to 70 min.

After 69 min, the GIWAXS signal from the metal halide template has vanished and the conversion is considered as completed. Entering stage four, heating is stopped, and the chamber is opened to ambient air. This stage mimics the condition when the substrate is removed from the POPOP deposition chamber. We observe that the PL peak emission energy decreases and that the intensity increases. A possible explanation of the PL emission position redshift could be the cooling of the substrate,[34] while the increased PL intensity can be ascribed to a lower degree of electron–phonon scattering as the temperature decreases.[35]

Toward the end of stage three, we observe an additional signal at 0.71 Å^{-1}, arising from an excess organohalide phase,[36] not to be confused with the metal halide template signal at 0.69 Å^{-1}. The latter, already visible in underconverted perovskite films as presented in Figure 2, stems from clusters of δ-$CsPbI_2Br$,[37,38] likely created during the co-evaporation of PbI_2 and CsBr. A comparison is shown in Figure S14 (Supporting Information).

Beyond tracking the growth, the orientation relative to the substrate - and how it evolves during conversion - can be inferred from the GIWAXS data, displayed in Figure S15. The template signal at 0.69 Å^{-1} and the signal at 0.71 Å^{-1} in stage four (overconverted) follow the orientation of the lead iodide and perovskite phases, respectively. The two template-related signals indicate a preferential orientation facing up with respect to the substrate, typical of the nanoplatelets obtained when evaporating metal halides.[39–41] The cubic perovskite phase, dominantly oriented face up at the start of the growth, transforms into a preferential face and corner-up orientation during the conversion.[42,43] The fact that the excess organohalide signal follows the perovskite's orientation suggests that it is behaving as a 2D-like phase growing on the perovskite facets, likely forming a structure close to FA_2PbI_4.[44]

As detailed in Figure S16 (Supporting Information), this low angle "organohalide excess" perovskite phase appears to be correlated with NH_4I content in the thin films, as determined by FTIR and NMR. A notable exception is observed with the PTFE hollow cube, introduced as proof of concept in the last section. Overconverted films obtained with this holder and the presented process do not show NH_4I in the thin films. The influence of the holders' material on thin film growth is discussed in the Section: *Influence of chemical environment* (Supporting Information).

Having identified the four conversion stages, where the last stage presents the transition into an overconverted film, we further investigated how different process parameters impact the different conversion regimes.

4. Conversion Regimes

We created a process condition matrix in which we varied the precursor quantity (FAI powder mass), the process duration, and substrate to precursor distance (height of the hollow cube), displayed in **Figure 4**. Importantly, the substrate to precursor distance (between 5 and 15 mm) did not result in temperature changes at the substrate level, measured as ca. 150°C when the

16146840, 2024, 10, Downloaded from https://onlinelibrary.wiley.com/doi/10.1002/aenm.202303423 by Universitã¤tsbibliothek Tã¼bingen, Wiley Online Library on [08/03/2024]. See the Terms and Conditions (https://onlinelibrary.wiley.com/terms-and-conditions) on Wiley Online Library for rules of use; OA articles are governed by the applicable Creative Commons License

16146840, 2024, 10, Downloaded from https://onlinelibrary.wiley.com/doi/10.1002/aenm.202303423 by Universitã¤tsbibliothek Tã¼bingen, Wiley Online Library on [08/03/2024]. See the Terms and Conditions (https://onlinelibrary.wiley.com/terms-and-conditions) on Wiley Online Library for rules of use; OA articles are governed by the applicable Creative Commons License

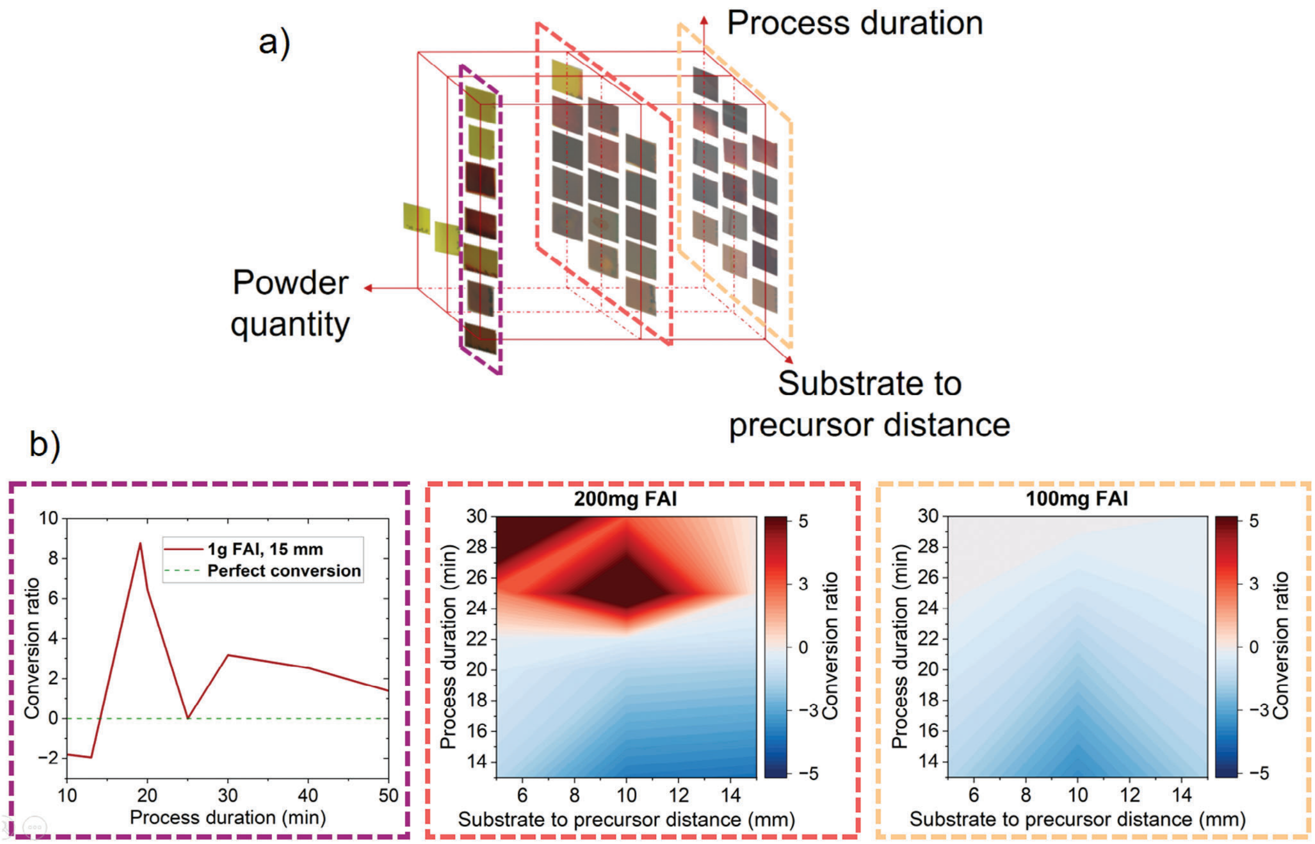

Figure 4. a) Experimental space explored. b) Exemplary evolution of the conversion ratio along different paths of the experimental space. In left plot (resp. middle and right contour plot), the perfect conversion objective is denoted with a green dash line (resp. white area).

heated table is set to 191°C, irrespective of the substrate to precursor distance.

This temperature gradient, bound to the holder design and not varied in this study, must be carefully considered when developing a vapor deposition process. Increasing the substrate temperature will favor diffusion of organohalide species in the metallic template but reduce condensation of organic species.[12,13,45] A compromise, specific to the process and the deposition setup, must be found to reach optimal deposition conditions.

To compare the different conversion regimes, we define a conversion ratio (CR) as:

$$CR = \begin{cases} \dfrac{\int_{OHal} \phi(i,j)\ d\theta}{\int_{Pk} \phi(i,j)\ d\theta} \cdot \dfrac{max_{j,\forall i}(\int_{Pk} \phi(i,j)\ d\theta)}{max_{j,\forall i}(\int_{OHal} \phi(i,j)\ d\theta)} > 0 & \text{if overconverted} \\ 0, & \text{if perfectly converted} \\ -\dfrac{\int_{Template} \phi(i,j)\ d\theta}{\int_{Pk} \phi(i,j)\ d\theta} \cdot \dfrac{max_{j,\forall i}(\int_{Pk} \phi(i,j)\ d\theta)}{max_{j,\forall i}(\int_{Template} \phi(i,j)\ d\theta)} < 0 & \text{if underconverted} \end{cases} \tag{1}$$

With $\phi(i, j)$ being the background-removed XRD signal of a phase (OHal: organohalide, Pk: perovskite or template) for a given process duration i and substrate to precursor distance j. Signals are normalized with respect to their maximum values (selected in the dataset with the same powder mass and substrate to precursor distance, with varying process durations) to account for the fact that the diffraction signal from the template is orders of magnitude higher than the signal from the excess organohalide, and thus give a proper feeling of severe overconversion cases.

The precursor quantity is the dominant driver of all changes and allows tuning the reaction kinetics in order to obtain different conversion regimes. While higher quantities of FAI (1g, 200 mg) favor a monotonous evolution of the conversion ratio, with signs of overconversion promptly visible after complete conversion, lesser FAI quantity (100mg) provides a more converging evolution of the conversion ratio (Figure 4b). With a smaller materials availability, the substrate balances the transport of material partially through re-evaporation, enabling more control, albeit at the cost of speed. Morphologically, the domains first form small rough domains in underconverted films that then transform into medium-sized flatter domains in perfectly converted films, followed by further growth into large flat grains in overconverted films (Figure S17a, Supporting Information). At the same time, the XRD patterns show the presence of the metal halide template (underconverted), a clean perovskite (optimum) to additional signals from the excess organohalides (overconverted), Figure S17b (Supporting Information). Despite these differences in morphology and crystallography, we did not observe signs of NH_4I in the NMR spectra, cf Figure S17c (Supporting Information). The in situ study of the previous section was realized with 300mg of FAI per run. The aforementioned results are coherent with the saturating conversion regime identified in this section. However, we want to highlight here that the more 'optimal' process

© 2024 Wiley-VCH GmbH

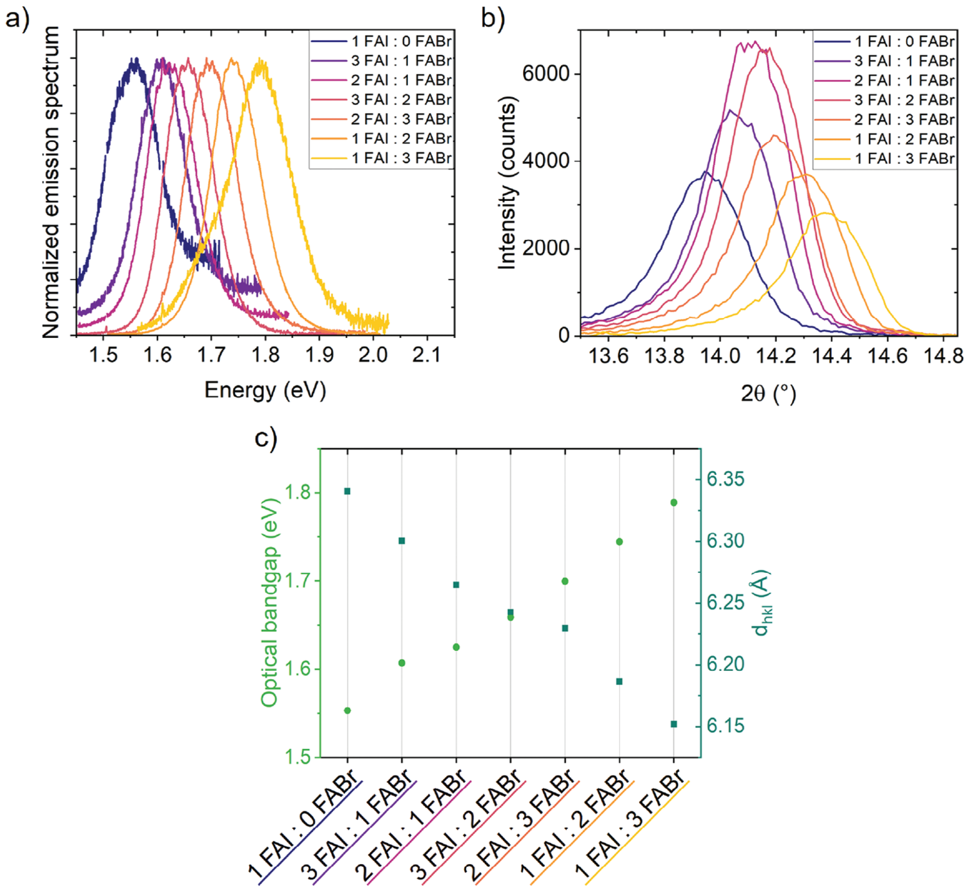

Figure 5. a) Bandgap tuning of the thin films, mixing FAI and FABr in precursors. Normalized emission spectra, b) perovskite (001) diffraction peak and c) corresponding optical bandgap and interplanar distance, respectively.

conditions identified in the current section are highly dependent on the holder and the organohalide source used, and will consequently evolve with the two latter in the following sections.

With the different conversion regimes identified and how they depend on process parameters, we sought to expand the toolset by exploring the possibility of tuning the composition of the final perovskite through the addition of mixed organohalide powders or alternative additives.

5. Bandgap Tuning and Additive Engineering

One of the properties that makes halide perovskites interesting for photovoltaic applications in (multi-junction) solar cells is their tunable bandgap. We explore the possibility of tuning the bandgap in the POPOP process. Exemplary, we mix FAI and formamidinium bromide (FABr) precursors and adapt the deposition parameters for optimal conversion. From now on, the presented results are obtained with the POPOP holder and procedure presented in Figure S17 (Supporting Information). This new prototype, now holding four substrates at the same time, features a rough (textured) silicon wafer as scaffold for organohalide source. The organohalide salts or potential additives are dissolved in ethanol, then dispersed and dried on the rough surface, hence forming a homogeneous organohalide source. A new holder being a substantial change in experimental conditions (like other process parameters: material quantity, temperatures, etc.), it must be kept in mind that the absolute numbers presented in the previous sections (e.g., time needed for complete perovskite conversion) are intrinsically bounded to a specific experimental setup. All experimental details are available in the Experimental Section and Figure S18 (Supporting Information).

As displayed in **Figure 5**, the photoluminescence peak position can be shifted controllably from 1.55 to 1.8 eV when varying the relative amounts of FAI: FABr. The optical bandgap variation is cross-checked with changes in the lattice d-spacing to exclude optical effects. Notably, we did not probe the degree/speed of phase segregation in the mixed-halide films but assume these films behave analogous to films processed using different solution- or vapor-deposition methods, i.e., showing phase segregation upon prolonged illumination. Introducing FABr accelerates the perovskite conversion and notably increases the optoelectronic quality (PLQY) of the films, Figure S19a (Supporting Information). The first apparent improvement in crystallinity of perovskite peak (Figure 5b) from 1 FAI: 0 FABr to 2 FAI: 1 FABr is explained by a more complete conversion into perovskite (diffractograms full range available Figure S19a, Supporting Information). Increasing further the Br content in the mix above 3 FAI: 2 FABr ratio (full perovskite conversion is reached at this point) decreases perovskite crystallinity, as visible from the diminishing peak intensity and the increasing full width at half maximum of the

16146840, 2024, 10, Downloaded from https://onlinelibrary.wiley.com/doi/10.1002/aenm.202303423 by Universitä¤tsbibliothek Tã¼Bingen, Wiley Online Library on [08/03/2024]. See the Terms and Conditions (https://onlinelibrary.wiley.com/terms-and-conditions) on Wiley Online Library for rules of use; OA articles are governed by the applicable Creative Commons License

signal. The 2.67 FAI: 1 FABr mix, with total equivalent mass of organohalide salts of 50mg (methodology described in Experimental Section), chosen as baseline for the following studies, gives an optical bandgap of 1.63 eV and converts within 9 min, with good homogeneity and repeatability, Figure S19b (Supporting Information). We chose the process parameters such that the reaction is in the self-limiting converging regime, as defined above. This increases the robustness: doubling the process time from 9 to 18 min does not lead to an oversaturation of the films.

However, a decrease in PLQY is observed as the process time increases. Also, the bandgap decreases with a longer process time (from 1.63 eV at 9 to 1.60 eV at 18 min of process) proceeding after the complete conversion into perovskite. In the POPOP process (holder loaded in chamber at temperature setpoint, organohalide salts mixed, dissolved and dried to form a homogeneous source, cf. Figure S18, Supporting Information and Experimental Section), the different salts generate respective organohalide vapors reacting with the metal halide template. FABr is present in a lesser quantity in the organohalide source, and its sublimation temperature is lower than FAI. The bromine source of the salts is consumed faster than the iodine one. This explains the redshift of the bandgap with prolonged exposure to the heated organohalide source, the influence of FAI vapors becoming dominant and provoking a halide exchange.[32,33]

One of the most common approaches to improve the performance of perovskite devices is to manipulate the growth via additives incorporation into the commonly solution-processed absorbers. For example, methylammonium chloride (MACl) is a popular choice for FA-based perovskites, allowing to tune perovskite crystallization to obtain large, passivated, and high-quality domains.[46] To demonstrate the feasibility of using MACl, we mixed it with our 2.67 FAI: 1 FABr baseline precursor composition (1.3 to 14% atomic MACl content relative to the total FAX organohalide). Figure S20 (Supporting Information) displays XRD, PLQY, SEM, NMR, and Time-of-Flight Secondary Ion Mass Spectrometry (ToF-SIMS) of the perovskite films grown with different amounts of MACl. Notably, adding MACl did not result in drastic changes in the crystal structure, where the diffraction intensity is not notably impacted. The width of the (001) perovskite signal is mildly reduced, in line with the slight increase of the apparent domain size, reaching a maximum at 9.8% of MACl. We probed whether MA only impacts the film formation and thereafter evaporates or is incorporated into the perovskite. Indeed, we observe a signal from the methyl quadruplet in NMR, scaling with the relative amount of MACl in the precursor organohalide mix, up to a maximum at 9.8%. Analogously, we probed the presence of Cl^- in the film via ToF-SIMS and observed an increased signal with increasing amounts of MACl, however significantly higher than the signal changes in MA (as measured via NMR). This difference indicates that MA and Cl are not exclusively present as MACl. From the ToF-SIMS, we can deduce that the Cl appears to be distributed throughout the films and slightly more concentrated at the bottom interface. We observe a reduction in the PLQY upon increasing MACl, suggesting non-radiative recombination. A possible explanation could be the decomposition of MACl into MA and HCl[47] when heated. This would rationalize the different amounts of MA and Cl and explain the lower optoelectronic quality, potentially due to deterioration upon uncontrolled HCl exposure.

The report by Zhao *et al.*[48] suggests that when MACl is used in a post-processing step after the conversion as a vapor treatment, with dedicated process conditions, it can aid in promoting better optoelectronic performances.

Alternatively, we added formamidinium thiocyanate (FASCN) to the FAI/FABr baseline mix, inspired by recent demonstrations of vapor-assisted crystallization.[49] In their work, Lu *et al.* deduce from ^{14}N solid-sate NMR measurement that the SCN^- ion is not incorporated into the lattice and rather lies at domain boundaries. Additionally, their molecular dynamic simulations suggest that the SCN^- ions preferentially react with the surface of non-photoactive δ-$FAPbI_3$, where the sulfur of the additive anion coordinates with the Pb^{2+} cation. This provokes a displacement of the halide and the disassembling of the external surface of the face-sharing octahedra structure, inducing a transition into a corner-sharing architecture of photoactive α-$FAPbI_3$. These simulations corroborate their experimental results showing that the thiocyanate ion favors the formation of highly crystalline and pure photoactive α-FA perovskite with bigger domains.

As displayed in **Figure 6a**, adding FASCN to the organohalide source of the POPOP process increases crystallinity (more pronounced diffraction intensity, reduced peak width) and PLQY. At the same time, the domains appear larger and flatter, Figure 6b. Up to ca. 8% FASCN, the morphology, crystallinity, and optoelectronic quality (measured through PLQY) improve unison, where a further increase beyond 9% results in the formation of pinholes in the thin film and a loss of crystallinity and PLQY.

ToF-SIMS measurements in Figure S21 (Supporting Information) reveal that the SCN^- ions are distributed throughout the perovskite film thickness in comparable quantities in all cases. This suggests that a self-limited amount of the additive during vapor exposure is incorporated while the 'excess' continues to influence the deposition without being absorbed by the growing film. Additionally, we observe a preferential accumulation at the bottom interface.

6. Photovoltaic Devices

Photovoltaic devices are fabricated to investigate the potential of the presented process. For all devices, the structure is Glass/ITO/MeO-2PACz/Perovskite/C_{60}/SnO_2/Ag. Figure S22 (Supporting Information) shows an optimization of the process duration for the 2.67 FAI: 1 FABr baseline and an investigation of MACl and FASCN additives' effect on devices. The latter results follow the trends of PLQY measurements: MACl as a vapor additive consistently worsens photovoltaic performances while adding 7.56% FASCN appears as the optimal concentration in the second series. The best device, whose JV curve and photovoltaic characteristics are displayed in **Figure 7b**, shows very low hysteresis at our standard scan speed of ≈ 100 mVs^{-1} and a high fill factor exceeding 80%. Devices made from films grown with higher FASCN content exhibit substantially reduced open circuit voltages and fill factors, likely due to the formation of the above-mentioned pinholes. The statistics of FASCN-containing cells, in Figure 7a, reveal that gains in PLQY are not directly translated into device performance, where the optimal FASCN content (cf. PLQY, XRD, see above) results in only minor improvements in the devices compared to the six times higher PLQY. This suggests

© 2024 Wiley-VCH GmbH

16146840, 2024, 10, Downloaded from https://onlinelibrary.wiley.com/doi/10.1002/aenm.202303423 by Universitä-Tsbibliothek Tä¼Binge, Wiley Online Library on [08/03/2024]. See the Terms and Conditions (https://onlinelibrary.wiley.com/terms-and-conditions) on Wiley Online Library for rules of use; OA articles are governed by the applicable Creative Commons License

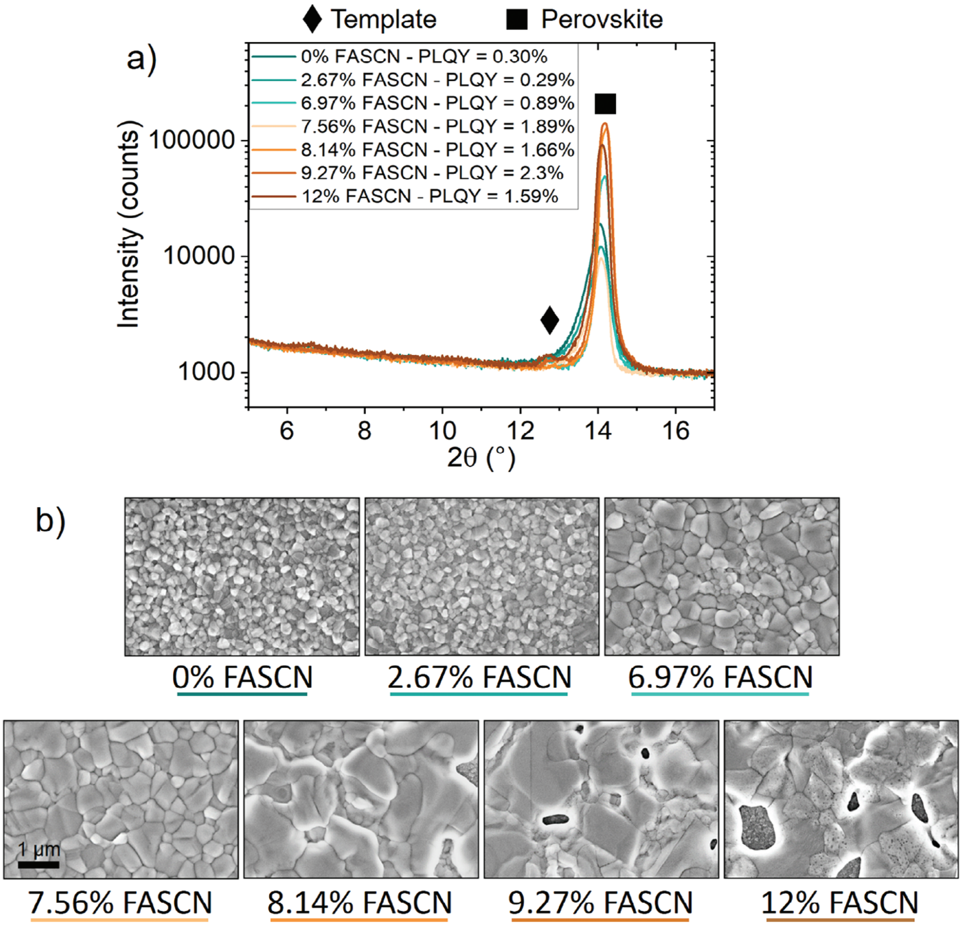

Figure 6. a) Effects of FASCN additive on PLQY and X-ray diffraction of the films. b) Top view SEM images of thin films with different amounts of FASCN. Scale is common to all images.

additional losses due to the transport layers and is confirmed by the loss study in Figure S24 (Supporting Information) showing that the perovskite/C_{60} interface is causing additional losses compared to the perovskite on the ITO/SAM substrate alone, limiting possible efficiency gains. Using other self-assembled monolayers, such as Me-4PACz, known to have a higher hole transfer efficiency,[50] adding interlayers between the perovskite and C_{60} to reduce non-radiative losses or improving the light-harvesting efficiency (exemplary external quantum efficiency measurements in Figure S23, Supporting Information), e.g., through anti-reflective

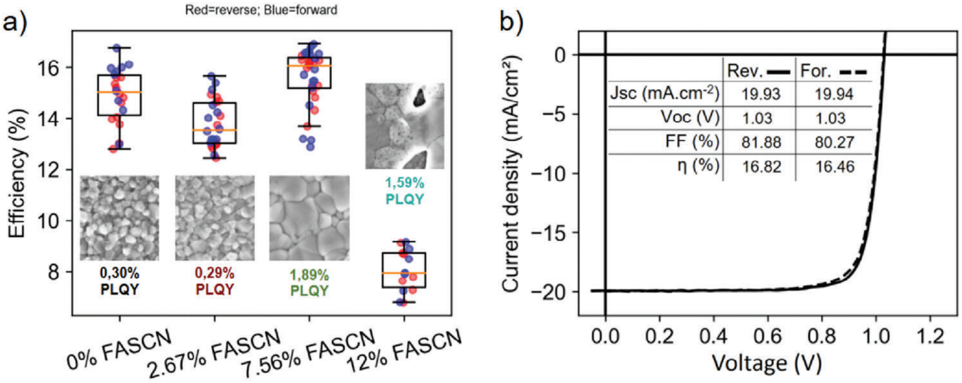

Figure 7. a) Photovoltaic devices with increasing FASCN content in the source. SEM images available in Figure 6 with full area and scale. b) Current density – Voltage curve of the best-performing device (7.56% FASCN, 9 minutes baseline, 2.67 FAI: 1 FABr, optical bandgap of 1.63 eV).

16146840, 2024, 10, Downloaded from https://onlinelibrary.wiley.com/doi/10.1002/aenm.202303423 by Universitã¤tsbibliothek Tã¼bingen, Wiley Online Library on [08/03/2024]. See the Terms and Conditions (https://onlinelibrary.wiley.com/terms-and-conditions) on Wiley Online Library for rules of use; OA articles are governed by the applicable Creative Commons License

coatings, will likely enable significant efficiency improvements beyond the herein shown proof of concept.

7. Conclusion

An evolution of close space sublimation of organohalides for perovskite thin film deposition is proposed. The developed process is fast, simple, controllable, repeatable, and upscalable. Halide tuning, as well as additive engineering, common in solution processing but rare in vapor depositions (or via post-treatment), are demonstrated and offer numerous possibilities. The process, consisting of four stages, is analyzed both in and ex situ from a structural, optoelectronic and chemical point of view. Key insights regarding the influence of the chemical environment on thin film growth are provided, and the importance of mechanical design is discussed. Photovoltaic devices proving the repeatability and potential of the process are demonstrated.

Further development of the process toward commercialization should focus on the following points: 1) further optimization of the overall process time (while the proof of concept organohalide deposition demonstrated here is already performed within 9 min, the metal halide deposition is still long and must also be optimized), 2) upscale further the deposition with adequate holders prototypes, 3) implement perovskite results in perovskite-silicon tandem solar cells (very promising for market penetration from a levelized cost of electricity point of view[51–55]) and 4) investigate device stability.

Supporting Information

Supporting Information is available from the Wiley Online Library or from the author.

Acknowledgements

The authors acknowledge funding from the European Union's Horizon 2020 research and innovation program (VIPERLAB, 101006715; TRIUMPH, 101075725 ; EPFLeaders4Impact, 10103; MSCA, 945363), the Swiss National Science Foundation (PAPET, 200021_197006; A3P, 40B2-0_1203626), the Swiss Federal Office of Energy (PRESTO, PERSISTARS), and the ETH Board through an SFA-AM grant (AMYS). This research was supported by the Czech Ministry of Education, Youth and Sports (LUASK 22202). The authors acknowledge the support of the Slovak Research and Development Agency (SK-CZ-RD-21-0043 and APVV-21-0297 F. S. wishes to thank the DFG and the BMBF. D.T. wishes to thank the Swiss State Secretary for Education, Research and Innovation for a FCS/ESKAS Swiss Government Excellence Scholarship. .

Conflict of Interest

The authors declare no conflict of interest.

Data Availability Statement

The data that support the findings of this study are available from the corresponding author upon reasonable request.

Keywords

in situ GIWAXS & PL, NMR, organohalides, perovskite growth, perovskite, photovoltaics, PLQY, thin films, ToF SIMS, vapor deposition

Received: October 10, 2023
Revised: December 15, 2023
Published online: February 2, 2024

[1] S. Albrecht, M. Saliba, J. Correa Baena, F. Lang, L. Kegelmann, M. Mews, L. Steier, A. Abate, J. Rappich, L. Korte, R. Schlatmann, M. Nazeeruddin, A. Hagfeldt, M. Grätzel, B. Rech, *Energy Environ. Sci.* **2016**, *9*, 81.
[2] F. Fu, T. Feurer, T. Jäger, E. Avancini, B. Bissig, S. Yoon, S. Buecheler, A. N. Tiwari, *Nat. Commun.* **2015**, *6*, 8932.
[3] J. H. Noh, S. H. Im, J. H. Heo, T. N. Mandal, S. I. Seok, *Nano Lett.* **2013**, *13*, 1764.
[4] Z. Li, M. Yang, J. S. Park, S. H. Wei, J. J. Berry, K. Zhu, *Chem. Mater.* **2016**, *28*, 284.
[5] National Renewable Energy Laboratory, Best research-cell efficiency chart, https://www.nrel.gov/pv/cell-efficiency.html (accessed: September, 1st **2023**).
[6] VDMA, International Technology Roadmap for Photovoltaic (ITRPV), Technical report, https://www.vdma.org/international-technology-roadmap-photovoltaic (accessed: September, 1st **2023**).
[7] M. J. Bækbo, O. Hansen, I. Chorkendorff, P. C. K. Vesborg, *RSC Adv.* **2018**, *8*, 29899.
[8] D. P. Nenon, J. A. Christians, L. M. Wheeler, J. L. Blackburn, E. M. Sanehira, B. Dou, M. L. Olsen, K. Zhu, J. J. Berry, J. M. Luther, *Energy Environ. Sci.* **2016**, *9*, 2072.
[9] E. J. Juarez-Perez, Z. Hawash, S. R. Raga, L. K. Ono, Y. Qi, *Energy Environ. Sci.* **2016**, *9*, 3406.
[10] F. Sahli, Q. J.-M. A. Guesnay, N. Salsi, L. Duchêne, C. Ballif, Q. Jeangros, *Preprint*, https://infoscience.epfl.ch/record/288002?ln=en, **2021**.
[11] E. J. Juarez-Perez, L. K. Ono, Y. Qi, *J. Mater. Chem. A* **2019**, *7*, 16912.
[12] Q. Guesnay, F. Sahli, C. Ballif, Q. Jeangros, *APL Mater.* **2021**, *9*, 100703.
[13] F. Sahli, N. Miaz, N. Salsi, C. Bucher, A. Schafflützel, Q. Guesnay, L. Duchêne, B. Niesen, C. Ballif, Q. Jeangros, *ACS Appl. Energy Mater.* **2021**, *4*, 4333.
[14] R. C. Powell, First Solar, L. L. C., Perrysburg, O. **2006**, 1. https://www.osti.gov/biblio/881482
[15] R. R. Lunt, B. E. Lassiter, J. B. Benziger, S. R. Forrest, *Appl. Phys. Lett.* **2009**, *95*, 2007.
[16] B. McCandless, R. Birkmire, W. Buchanan, in *Conference Record of the Twenty-Ninth IEEE Photovoltaic Specialists Conference, 2002*, IEEE, Piscataway, NJ **2002**, pp. 547–550.
[17] Q. Guesnay, C. J. McMonagle, D. Chernyshov, W. Zia, A. Wieczorek, S. Siol, M. Saliba, C. Ballif, C. M. Wolff, *ACS Photonics* **2023**, *10*, 3087.
[18] A. Greco, A. Hinderhofer, M. I. Dar, N. Arora, J. Hagenlocher, A. Chumakov, M. Grätzel, F. Schreiber, *J. Phys. Chem. Lett.* **2018**, *9*, 6750.
[19] V. Held, N. Mrkyvkova, P. Nádaždy, K. Vegso, A. Vlk, M. Ledinský, M. Jergel, A. Chumakov, S. V. Roth, F. Schreiber, P. Siffalovic, *J. Phys. Chem. Lett.* **2022**, *13*, 11905.
[20] N. Mrkyvkova, V. Held, P. Nádaždy, R. Subair, E. Majkova, M. Jergel, A. Vlk, M. Ledinsky, M. Kotlár, J. Tian, P. Siffalovic, *J. Phys. Chem. Lett.* **2021**, *12*, 10156.
[21] A few adjustments to the sample holder were made. The main change consists of two lateral X-ray transparent windows in polyimide (PI), to allow the primary X-ray beam to reach the forming perovskite layer facing down, and let the diffracted beams reach the X-ray detector. The holder is also slightly higher (2 cm substrate to precursor distance) to grant a sufficient solid angle for X-ray collection. A schematic of the holder, as well as pictures describing the experimental setup, are available in Figure S10 (Supporting Information). The process parameters were chosen to mimic conditions in the

© 2024 Wiley-VCH GmbH

16146840, 2024, 10, Downloaded from https://onlinelibrary.wiley.com/doi/10.1002/aenm.202303423 by Universitã¤Tsbibliothek Tã¼Binge, Wiley Online Library on [08/03/2024]. See the Terms and Conditions (https://onlinelibrary.wiley.com/terms-and-conditions) on Wiley Online Library for rules of use; OA articles are governed by the applicable Creative Commons License

original reaction chamber: layer stack, pressure, temperature, geometry, materials used etc. Experimental details are available in the Methods section of the Supporting Information.

[22] S. Svanström, A. García Fernández, T. Sloboda, T. J. Jacobsson, H. Rensmo, U. B. Cappel, *Phys. Chem. Chem. Phys.* **2021**, *23*, 12479.

[23] Reaching 190°C would have taken ca. 45 min.

[24] Y. Zhao, H. Tan, H. Yuan, Z. Yang, J. Z. Fan, J. Kim, O. Voznyy, X. Gong, L. N. Quan, C. S. Tan, J. Hofkens, D. Yu, Q. Zhao, E. H. Sargent, *Nat. Commun.* **2018**, *9*, 1.

[25] K. Suchan, J. Just, P. Becker, E. L. Unger, T. Unold, *J. Mater. Chem. A* **2020**, *8*, 10439.

[26] L. Wagner, L. E. Mundt, G. Mathiazhagan, M. Mundus, M. C. Schubert, S. Mastroianni, U. Würfel, A. Hinsch, S. W. Glunz, *Sci. Rep.* **2017**, *7*, 1.

[27] E. S. Parrott, J. B. Patel, A. A. Haghighirad, H. J. Snaith, M. B. Johnston, L. M. Herz, *Nanoscale* **2019**, *11*, 14276.

[28] J. A. Steele, E. Solano, D. Hardy, D. Dayton, D. Ladd, K. White, P. Chen, J. Hou, H. Huang, R. A. Saha, L. Wang, F. Gao, J. Hofkens, M. B. J. Roeffaers, D. Chernyshov, M. F. Toney, *Adv. Energy Mater.* **2023**, *13*, 2300760.

[29] G. W. Adhyaksa, S. Brittman, H. Āboliņš, A. Lof, X. Li, J. D. Keelor, Y. Luo, T. Duevski, R. M. Heeren, S. R. Ellis, D. P. Fenning, E. C. Garnett, *Adv. Mater.* **2018**, *30*, 52.

[30] A. D. Wright, G. Volonakis, J. Borchert, C. L. Davies, F. Giustino, M. B. Johnston, L. M. Herz, *Nat. Mater.* **2020**, *19*, 1201.

[31] L. Brus, *J. Phys. Chem.* **1986**, *90*, 2555.

[32] M. Long, T. Zhang, W. Xu, X. Zeng, F. Xie, Q. Li, Z. Chen, F. Zhou, K. S. Wong, K. Yan, J. Xu, *Adv. Energy Mater.* **2017**, *7*, 1601882.

[33] G. Li, J. Y. L. Ho, M. Wong, H. S. Kwok, *J. Phys. Chem. C* **2015**, *119*, 26883.

[34] H. Zheng, J. Dai, J. Duan, F. Chen, G. Zhu, F. Wang, C. Xu, *J. Mater. Chem. C* **2017**, *5*, 12057.

[35] A. D. Wright, C. Verdi, R. L. Milot, G. E. Eperon, M. A. Pérez-Osorio, H. J. Snaith, F. Giustino, M. B. Johnston, L. M. Herz, *Nat. Commun.* **2016**, *7*, 11755.

[36] M. R. Leyden, M. V. Lee, S. R. Raga, Y. Qi, *J. Mater. Chem. A* **2015**, *3*, 16097.

[37] J. K. Nam, M. S. Jung, S. U. Chai, Y. J. Choi, D. Kim, J. H. Park, *J. Phys. Chem. Lett.* **2017**, *8*, 2936.

[38] C. Liu, W. Li, C. Zhang, Y. Ma, J. Fan, Y. Mai, *J. Am. Chem. Soc.* **2018**, *140*, 3825.

[39] F. Fu, L. Kranz, S. Yoon, J. Löckinger, T. Jäger, J. Perrenoud, T. Feurer, C. Gretener, S. Buecheler, A. N. Tiwari, *Phys. Status Solidi (A) Appl. Mater. Sci.* **2015**, *212*, 2708.

[40] A. Koffman-Frischknecht, M. Soldera, F. Soldera, M. Troviano, L. Carlos, M. D. Perez, K. Taretto, *Thin Solid Films* **2018**, *653*, 249.

[41] H. Hu, D. Wang, Y. Zhou, J. Zhang, S. Lv, S. Pang, X. Chen, Z. Liu, N. P. Padture, G. Cui, *RSC Adv.* **2014**, *4*, 28964.

[42] L. Oesinghaus, J. Schlipf, N. Giesbrecht, L. Song, Y. Hu, T. Bein, P. Docampo, P. Müller-Buschbaum, *Adv. Mater. Interfaces* **2016**, *3*, 1600403.

[43] L. Wang, X. Wang, L. Zhu, S. B. Leng, J. Liang, Y. Zheng, Z. Zhang, Z. Zhang, X. X. Liu, F. Liu, C. C. Chen, *Chem. Eng. J.* **2022**, *430*, 132730.

[44] X. Zhu, Z. Xu, S. Zuo, J. Feng, Z. Wang, X. Zhang, K. Zhao, J. Zhang, H. Liu, S. Priya, S. F. Liu, D. Yang, *Energy Environ. Sci.* **2018**, *11*, 3349.

[45] K. B. Lohmann, J. B. Patel, M. U. Rothmann, C. Q. Xia, R. D. J. Oliver, L. M. Herz, H. J. Snaith, M. B. Johnston, *ACS Energy Lett.* **2020**, *5*, 710.

[46] K. Odysseas Kosmatos, L. Theofylaktos, E. Giannakaki, D. Deligiannis, M. Konstantakou, T. Stergiopoulos, *Energy Environ. Mater.* **2019**, *2*, 79.

[47] A. E. Williams, P. J. Holliman, M. J. Carnie, M. L. Davies, D. A. Worsley, T. M. Watson, *J. Mater. Chem. A* **2014**, *2*, 19338.

[48] F. Zhao, J. Zhong, L. Zhang, P. Yong, J. Lu, M. Xu, Y.-b. Cheng, Z. Ku, *Solar RRL* **2023**, *7*, 11.

[49] H. Lu, Y. Liu, P. Ahlawat, A. Mishra, W. R. Tress, F. T. Eickemeyer, Y. Yang, F. Fu, Z. Wang, C. E. Avalos, B. I. Carlsen, A. Agarwalla, X. Zhang, X. Li, Y. Zhan, S. M. Zakeeruddin, L. Emsley, U. Rothlisberger, L. Zheng, A. Hagfeldt, M. Grätzel, *Science* **2020**, *370*, 6512.

[50] I. Levine, A. Al-Ashouri, A. Musiienko, H. Hempel, A. Magomedov, A. Drevilkauskaite, V. Getautis, D. Menzel, K. Hinrichs, T. Unold, S. Albrecht, T. Dittrich, *Joule* **2021**, *5*, 2915.

[51] M. T. Hörantner, T. Leijtens, M. E. Ziffer, G. E. Eperon, M. G. Christoforo, M. D. McGehee, H. J. Snaith, *ACS Energy Lett.* **2017**, *2*, 2506.

[52] S. Altazin, L. Stepanova, J. Werner, B. Niesen, C. Ballif, B. Ruhstaller, *Opt. Express* **2018**, *26*, A579.

[53] J. Werner, B. Niesen, C. Ballif, *Adv. Mater. Interfaces* **2018**, *5*, 1.

[54] J. Lehr, M. Langenhorst, R. Schmager, S. Kirner, U. Lemmer, B. S. Richards, C. Case, U. W. Paetzold, *Sustainable Energy Fuels* **2018**, *2*, 2754.

[55] Z. J. Yu, J. V. Carpenter, Z. C. Holman, *Nat. Energy* **2018**, *3*, 747.

© 2024 Wiley-VCH GmbH

16146840, 2024, 10, Downloaded from https://onlinelibrary.wiley.com/doi/10.1002/aenm.202303423 by Universitã¤tsbibliothek Tã¼binge, Wiley Online Library on [08/03/2024]. See the Terms and Conditions (https://onlinelibrary.wiley.com/terms-and-conditions) on Wiley Online Library for rules of use; OA articles are governed by the applicable Creative Commons License